INSTITUTE OF PHYSICS PUBLISHING PHYSICS IN MEDICINE AND BIOLOGY

Phys. Med. Biol. **48** (2003) 3101–3116 PII: S0031-9155(03)63003-4

Conductivity and current density image reconstruction using harmonic B_z algorithm in magnetic resonance electrical impedance tomography

Suk Hoon Oh[1], Byung Il Lee[2], Eung Je Woo[2], Soo Yeol Lee[1], Min Hyoung Cho[1], Ohin Kwon[3] and Jin Keun Seo[4]

[1] Graduate School of East–West Medical Sciences, Kyung Hee University, Korea
[2] College of Electronics and Information, Kyung Hee University, Korea
[3] Department of Mathematics, Konkuk University, Korea
[4] Department of Mathematics, Yonsei University, Korea

E-mail: ejwoo@khu.ac.kr

Received 2 May 2003, in final form 1 August 2003
Published 16 September 2003
Online at stacks.iop.org/PMB/48/3101

Abstract

Magnetic resonance electrical impedance tomography (MREIT) is to provide cross-sectional images of the conductivity distribution σ of a subject. While injecting current into the subject, we measure one component B_z of the induced magnetic flux density $\mathbf{B} = (B_x, B_y, B_z)$ using an MRI scanner. Based on the relation between $\nabla^2 B_z$ and $\nabla\sigma$, the harmonic B_z algorithm reconstructs an image of σ using the measured B_z data from multiple imaging slices. After we obtain σ, we can reconstruct images of current density distributions for any given current injection method. Following the description of the harmonic B_z algorithm, this paper presents reconstructed conductivity and current density images from computer simulations and phantom experiments using four recessed electrodes injecting six different currents of 26 mA. For experimental results, we used a three-dimensional saline phantom with two polyacrylamide objects inside. We used our 0.3 T (tesla) experimental MRI scanner to measure the induced B_z. Using the harmonic B_z algorithm, we could reconstruct conductivity and current density images with 82×82 pixels. The pixel size was 0.6×0.6 mm^2. The relative L^2 errors of the reconstructed images were between 13.8 and 21.5% when the signal-to-noise ratio (SNR) of the corresponding MR magnitude images was about 30. The results suggest that *in vitro* and *in vivo* experimental studies with animal subjects are feasible. Further studies are requested to reduce the amount of injection current down to less than 1 mA for human subjects.

1. Introduction

Cross-sectional imaging of electrical conductivity (or resistivity) distributions will be a valuable tool in diverse biomedical applications (Webster 1990). Electrical impedance tomography (EIT) provides conductivity images of the human body reconstructed from the measured boundary voltage data due to multiple injection currents through surface electrodes (Boone *et al* 1997, Saulnier *et al* 2001). In order to improve the spatial resolution and accuracy of the conductivity image, magnetic resonance electrical impedance tomography (MREIT) has been suggested (Zhang 1992, Woo *et al* 1994, Birgul and Ider 1995, Ider *et al* 1995, Ider and Birgul 1998, Eyuboglu *et al* 2001, Kwon *et al* 2002b). In MREIT, we use an MRI scanner to measure the induced magnetic flux density $\mathbf{B}$ due to an injection current I and utilize it to reconstruct cross-sectional conductivity images.

When all three components of $\mathbf{B} = (B_x, B_y, B_z)$ have been measured, we can compute the current density $\mathbf{J}$ inside the subject as $\mathbf{J} = \nabla \times \mathbf{B}/\mu_0$ where μ_0 is the magnetic permeability of the free space. This has been the research topic of magnetic resonance current density imaging (MRCDI) (Scott *et al* 1991, 1992, Eyuboglu *et al* 1998, Gamba *et al* 1999, Joy *et al* 1999). In previous MREIT studies where the internal current density $\mathbf{J}$ is utilized, image reconstruction algorithms such as the J-substitution algorithm (Kwon *et al* 2002b), current-constrained-voltage-scaled-reconstruction algorithm (Birgul *et al* 2003) and different forms of equipotential line methods (Eyuboglu *et al* 1999, Kwon *et al* 2002a, Ider *et al* 2003) have been suggested. Experimental results of the J-substitution algorithm using saline phantoms are described in Khang *et al* (2002), Oh *et al* (2002) and Lee *et al* (2003a). Eyuboglu and Ozdemir (2003) presented experimental results using a method based on equipotential projections.

However, at one time, we can measure only one component of $\mathbf{B}$ that is parallel to the direction of the main magnetic field of the MRI scanner. In this paper, we assume that the direction of the main magnetic field is the z-direction. After we obtain B_z, we must rotate the subject twice within the scanner to acquire B_x and B_y. This mechanical rotation procedure is clearly a major hurdle in practical applications of MRCDI and MREIT techniques.

Lately, Seo *et al* (2003) proposed a new conductivity image reconstruction technique based on the measurement of only B_z. Though this method does not require the impractical subject rotation procedure, it is based on the computation of $\nabla^2 B_z$. This means that we must differentiate noisy B_z images twice. Furthermore, their image reconstruction algorithm used line integrals to compute the conductivity σ from its spatial gradient $\nabla\sigma$, and line integrals tend to accumulate errors. Therefore, they could show only computer simulation results with a small amount of added noise.

This paper suggests an improved image reconstruction technique that can provide cross-sectional conductivity and current density images from noisy data of B_z. After describing the image reconstruction problem using multiple measurements of B_z, we will introduce a new algorithm called the harmonic B_z algorithm. The performance of the new technique will be shown using simulated B_z data with added Gaussian random noise of realistic amounts. We will also present conductivity and current density images of a saline phantom using measured B_z data from our 0.3 T experimental MRI scanner.

2. Methods

2.1. Description of image reconstruction problem using $\nabla^2 B_z$

We place a subject inside an MRI scanner and attach surface electrodes. Assuming that the number of electrodes is E, we can sequentially select one of $N = E(E-1)/2$ different

pairs of electrodes to inject current into the subject. Let the injection current between the jth pair of electrodes be I^j for $j = 1, \ldots, N$. The current I^j produces a current density $\mathbf{J}^j = \left(J_x^j, J_y^j, J_z^j\right)$ inside the subject. The presence of the internal current density $\mathbf{J}^j$ and the current I^j in external lead wires generates a magnetic flux density $\mathbf{B}^j = \left(B_x^j, B_y^j, B_z^j\right)$ and $\mathbf{J}^j = \nabla \times \mathbf{B}^j/\mu_0$ holds inside the electrically conducting subject. This induced magnetic flux density causes incremental changes in MR phase images that are proportional to B_z^j. We now assume that we have measured B_z^j from the corresponding MR phase images of the subject for $j = 1, \ldots, N$.

We assume that the conductivity distribution σ of the subject is isotropic with $0 < \sigma < \infty$. Let u^j be the voltage due to the injection current I^j for $j = 1, \ldots, N$. Since σ is approximately independent of injection currents, each u^j is a solution of the following classical boundary value problem:

$$\begin{cases} \nabla \cdot (\sigma \nabla u^j) = 0 \\ -\sigma \nabla u^j \cdot \mathbf{n} = g^j \end{cases} \tag{1}$$

where $\mathbf{n}$ is the outward unit normal vector and g^j is the normal component of current density on the boundary of the subject for the injection current I^j. Across a current injection electrode $\mathcal{E}$, we have $\int_{\mathcal{E}} g^j \, \mathrm{d}s = \pm I^j$ where the sign depends on the direction of current and g^j is zero on the regions of boundary not contacting with a chosen pair of current injection electrodes. The boundary value problem in (1) has a unique solution when we choose a ground or reference position with zero voltage. If σ, I^j and electrode configuration are given, we can solve (1) for u^j using numerical methods such as the finite element method (FEM).

From the z-component of the relation of $\nabla^2 \mathbf{B} = -\mu_0 \nabla u \times \nabla \sigma$ observed by Scott *et al* (1991), we can obtain

$$\frac{1}{\mu_0} \nabla^2 B_z^j = \left(\frac{\partial \sigma}{\partial x}, \frac{\partial \sigma}{\partial y} \right) \cdot \left(\frac{\partial u^j}{\partial y}, -\frac{\partial u^j}{\partial x} \right) \qquad j = 1, \ldots, N \tag{2}$$

for each position inside the subject. Using a matrix form, (2) becomes

$$\mathbf{U}\mathbf{s} = \mathbf{b} \tag{3}$$

where

$$\mathbf{U} = \begin{bmatrix} \frac{\partial u^1}{\partial y} & -\frac{\partial u^1}{\partial x} \\ \vdots & \vdots \\ \frac{\partial u^N}{\partial y} & -\frac{\partial u^N}{\partial x} \end{bmatrix} \qquad \mathbf{s} = \begin{bmatrix} \frac{\partial \sigma}{\partial x} \\ \frac{\partial \sigma}{\partial y} \end{bmatrix} \qquad \text{and} \qquad \mathbf{b} = \frac{1}{\mu_0} \begin{bmatrix} \nabla^2 B_z^1 \\ \vdots \\ \nabla^2 B_z^N \end{bmatrix}.$$

For the case where two injection currents are used ($N = 2$), we can obtain $\mathbf{s}$ provided that the two voltages u^1 and u^2 corresponding to the two injection currents I^1 and I^2 satisfy

$$-\frac{\partial u^1}{\partial y}\frac{\partial u^2}{\partial x} + \frac{\partial u^1}{\partial x}\frac{\partial u^2}{\partial y} \neq 0. \tag{4}$$

We can argue that (4) holds for almost all positions within the subject since the two current densities $\mathbf{J}^1$ and $\mathbf{J}^2$ due to appropriately chosen I^1 and I^2 will not have the same direction (Kim *et al* 2002, Ider *et al* 2003).

In this paper, we use N injection currents to better handle measurement noise in B_z with an averaging effect. Using the weighted regularized least square method, we can get $\mathbf{s}$ as

$$\mathbf{s} = (\tilde{\mathbf{U}}^T \tilde{\mathbf{U}} + \lambda \mathbf{I})^{-1} \tilde{\mathbf{U}}^T \tilde{\mathbf{b}} \tag{5}$$

where $\tilde{\mathbf{U}}^T$ is the transpose of $\tilde{\mathbf{U}}$, λ is a positive regularization parameter, $\mathbf{I}$ is the 2×2 identity matrix, $\tilde{\mathbf{U}} = \mathbf{W}\mathbf{U}$, $\tilde{\mathbf{b}} = \mathbf{W}\mathbf{b}$ and $\mathbf{W} = \mathrm{diag}(w_1, \ldots, w_N)$ is an $N \times N$ diagonal weight matrix.

There could be different ways of determining the value of λ and the weight w_j. One way of setting the value of λ is to make it inversely proportional to the absolute value of the determinant of $\tilde{\mathbf{U}}^T\tilde{\mathbf{U}}$. This means that we use a larger λ where all ∇u^j for $j = 1, \ldots, N$ have almost the same directions and/or all $|\nabla u^j|$ are small. For the weighting factor w_j, we may set

$$w_j = \frac{SNR_j}{\sum_{j=1}^{N} SNR_j} \tag{6}$$

where SNR_j is the signal-to-noise ratio (SNR) of the measured B_z^j. Note that SNR_j should be determined for each position or pixel. In practice, however, it is difficult to know SNR_j for each position. We will discuss how to estimate SNR_j from measured B_z^j data later in this paper. Computing (5) for each position or pixel, we obtain a distribution of $\mathbf{s} = \left[\frac{\partial\sigma}{\partial x} \quad \frac{\partial\sigma}{\partial y}\right]^T$ inside the subject.

We now tentatively assume that the imaging slice $\mathcal{S}$ is lying in the plane $\{z = 0\}$ and the conductivity value at a fixed position $\mathbf{r}_0 = (x_0, y_0, 0)$ on its boundary $\partial\mathcal{S}$ is 1. For a moment, we denote $\mathbf{r} = (x, y)$, $\mathbf{r}' = (x', y')$ and $\sigma(x, y, 0) = \sigma(\mathbf{r})$. In order to compute σ from $\nabla\sigma = \left(\frac{\partial\sigma}{\partial x}, \frac{\partial\sigma}{\partial y}\right)$, Seo *et al* (2003) suggested a method using line integrals. However, since the line integral technique tends to accumulate errors, it is not suitable for noisy B_z data. We, therefore, employ a layer potential technique in two dimensions. Then,

$$\begin{aligned}\sigma(\mathbf{r}) &= \int_{\mathcal{S}} \nabla^2\Phi(\mathbf{r} - \mathbf{r}')\sigma(\mathbf{r}')\,\mathrm{d}\mathbf{r}' \\ &= -\int_{\mathcal{S}} \nabla_{\mathbf{r}'}\Phi(\mathbf{r} - \mathbf{r}') \cdot \nabla\sigma(\mathbf{r}')\,\mathrm{d}\mathbf{r}' + \int_{\partial\mathcal{S}} \mathbf{n}_{\mathbf{r}'} \cdot \nabla_{\mathbf{r}'}\Phi(\mathbf{r} - \mathbf{r}')\sigma(\mathbf{r}')\,\mathrm{d}l_{\mathbf{r}'}\end{aligned} \tag{7}$$

where $\Phi(\mathbf{r} - \mathbf{r}') = \frac{1}{2\pi}\log|\mathbf{r} - \mathbf{r}'|$ and $\nabla_{\mathbf{r}'}\Phi(\mathbf{r} - \mathbf{r}') = -\frac{1}{2\pi}\frac{\mathbf{r}-\mathbf{r}'}{|\mathbf{r}-\mathbf{r}'|^2}$. It is well known (Folland 1976) that for $\mathbf{r} \in \partial\mathcal{S}$

$$\lim_{t\to+0}\int_{\partial\mathcal{S}} \mathbf{n}_{\mathbf{r}'} \cdot \nabla_{\mathbf{r}'}\Phi(\mathbf{r} - t\mathbf{n}_{\mathbf{r}} - \mathbf{r}')\sigma(\mathbf{r}')\,\mathrm{d}l_{\mathbf{r}'} = \frac{\sigma(\mathbf{r})}{2} + \int_{\partial\mathcal{S}} \mathbf{n}_{\mathbf{r}'} \cdot \nabla_{\mathbf{r}'}\Phi(\mathbf{r} - \mathbf{r}')\sigma(\mathbf{r}')\,\mathrm{d}l_{\mathbf{r}'}.$$

Hence, as $\mathbf{r} \in S$ approaches the boundary ∂S in (7), we have

$$\frac{\sigma_{\partial\mathcal{S}}(\mathbf{r})}{2} + \frac{1}{2\pi}\int_{\partial S} \frac{(\mathbf{r} - \mathbf{r}') \cdot \mathbf{n}_{\mathbf{r}'}}{|\mathbf{r} - \mathbf{r}'|^2}\sigma_{\partial\mathcal{S}}(\mathbf{r}')\,\mathrm{d}l'_{\mathbf{r}} = \frac{1}{2\pi}\int_{\mathcal{S}} \frac{(\mathbf{r} - \mathbf{r}') \cdot \nabla\sigma(\mathbf{r}')}{|\mathbf{r} - \mathbf{r}'|^2}\,\mathrm{d}\mathbf{r}' \tag{8}$$

where $\sigma_{\partial S}$ denotes the conductivity restricted at the boundary $\partial\mathcal{S}$. It is also well known that the solvability of the integral equation (8) for $\sigma_{\partial\mathcal{S}}$ is guaranteed for a given right-hand side of (8) (Folland 1976). Since $\nabla\sigma$ is known in $\mathcal{S}$, the right-hand side of (8) is known. This enables us to obtain the value $\sigma_{\partial S}$ by solving the integral equation (8). Now, we can compute the conductivity σ in $\mathcal{S}$ by substituting the boundary conductivity $\sigma_{\partial\mathcal{S}}$ into (7) as

$$\sigma(\mathbf{r}) = -\int_{\mathcal{S}} \nabla_{\mathbf{r}'}\Phi(\mathbf{r} - \mathbf{r}') \cdot \nabla\sigma(\mathbf{r}')\,\mathrm{d}\mathbf{r}' + \int_{\partial\mathcal{S}} \mathbf{n}_{\mathbf{r}'} \cdot \nabla_{\mathbf{r}'}\Phi(\mathbf{r} - \mathbf{r}')\sigma_{\partial\mathcal{S}}(\mathbf{r}')\,\mathrm{d}l_{\mathbf{r}'}. \tag{9}$$

The process of solving (5) for each pixel and (8) and (9) for each imaging slice can be repeated for all imaging slices of interest within the subject as long as the measured data B_z are available for the slices. Furthermore, we can apply the method described in this section to any imaging slice of axial, coronal and sagittal directions.

2.2. Image reconstruction algorithm: $\nabla^2 B_z$ algorithm

As expressed in (1), voltages u^j depend on the unknown true conductivity σ and, therefore, we do not know the matrix $\mathbf{U}$ corresponding to σ. This requires us to use the iterative

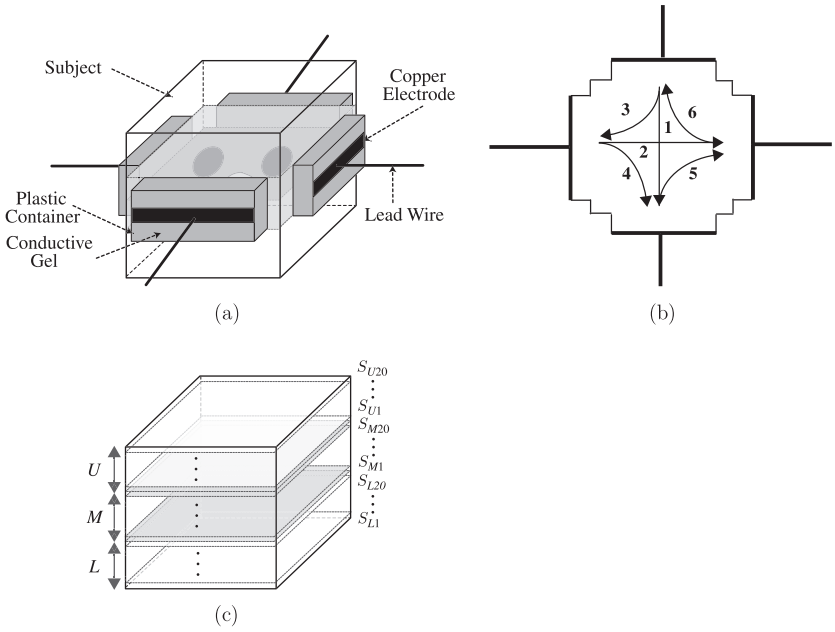

Figure 1. (a) Subject with four recessed electrodes used in computer simulations. (b) Six different injection currents (top view). (c) Definition of regions and slices.

algorithm described below. For $j = 1, \ldots, N$, we sequentially inject current I^j through a chosen pair of electrodes and measure the z-component of the induced magnetic flux density B_z^j from multiple imaging slices. For each injection current I^j, we also measure boundary voltages $u^j\,|_{\partial\mathcal{S}}$ on electrodes not injecting the current I^j. Then, the $\nabla^2 B_z$ algorithm is as follows:

Step 1. Let $m = 0$ and assume an initial conductivity distribution σ_0.
Step 2. Compute u_{m+1}^j by solving the following Neumann boundary value problems for $j = 1, \ldots, N$:

$$\begin{cases} \nabla \cdot \left(\sigma_m \nabla u_{m+1}^j\right) = 0 \\ -\sigma_m \nabla u_{m+1}^j \cdot \mathbf{n} = g^j. \end{cases} \tag{10}$$

Step 3. Compute σ_{m+1} using (5), (8) and (9). Scale σ_{m+1} using the measured boundary voltages $u^j|_{\partial\mathcal{S}}$ and the corresponding computed ones $u_{m+1}^j|_{\partial\mathcal{S}}$.
Step 4. If $\frac{\|\sigma_{m+1}-\sigma_m\|_2}{\|\sigma_{m+1}\|_2} < \epsilon$, go to step 5. Here, ϵ is a given tolerance. Otherwise, set $m \leftarrow (m+1)$ and go to step 2.
Step 5. Compute current density images as $\mathbf{J}^j \leftarrow -\sigma_{m+1}\nabla u_M^j$ where u_M^j is a solution of the boundary value problem in (1) with σ replaced by σ_{m+1}.

2.3. Computer simulation methods

Figure 1(a) shows an electrically conducting subject with an isotropic and piecewise constant conductivity distribution σ. The dimension of the subject is $50 \times 50 \times 50\ \text{mm}^3$. In order to inject currents into the subject, we may attach copper electrodes on the boundary of the subject. In real experiments, however, severe artefacts are produced in MR images near copper

electrodes due to RF shielding effects. The remedy is to use recessed electrodes. By recessing copper electrodes, we can effectively move these artefacts away from the boundary of the subject. Since we used recessed electrodes in real experiments described in the next section, we also used them in computer simulations. Figure 1(a) shows the subject with four recessed electrode assemblies of $10 \times 33.3 \times 16.7$ mm^3. With four electrodes of 33.3×16.7 mm^2 installed in the recessed electrode assemblies, we inject six currents between six different pairs of electrodes as shown in figure 1(b).

For the discretization of the model including the subject and four recessed electrode assemblies into a finite element mesh, we used eight-node hexahedral elements with trilinear interpolation functions. Each hexahedral element was $0.83 \times 0.83 \times 0.83$ mm^3 and the mesh included $60 \times 60 \times 60$ elements for the subject and $12 \times 40 \times 20$ elements for each recessed electrode assembly. There were a total of 254 400 elements and 268 309 nodes. The origin was located at the centre of the mesh.

As shown in figure 1(c), we denote three regions of the subject as L, M and U. There are 20 slices in each region and the thickness of each slice is 0.83 mm. We denote slices in L, M and U as $\mathcal{S}_{L_i}$, $\mathcal{S}_{M_i}$ and $\mathcal{S}_{U_i}$, respectively, for $i = 1, \ldots, 20$ from the lowest to the highest slice. We set the conductivity distribution of the region M as a target conductivity distribution to be imaged. The conductivity distributions of L and U were different from that of M to simulate a general three-dimensional conductivity distribution without any symmetry in all three directions.

For each injection current I^j of 26 mA, we computed the z-component of the induced magnetic flux density B_z^j for $j = 1, \ldots, 6$ using a three-dimensional forward solver (Lee *et al* 2002, 2003b). Instead of computing B_z^j for all 60 slices, we computed them only in 20 slices $\mathcal{S}_{M_i}$ of the region M. This simulates practical situations where we acquire MR images from a portion of the subject. For the computation of $\nabla^2 B_z$ at the ith pixel, we used the simple three-point difference scheme as

$$\begin{aligned}\nabla^2 B_z(x_i, y_i, z_i) = {} & \frac{B_z(x_{i+1}, y_i, z_i) - 2B_z(x_i, y_i, z_i) + B_z(x_{i-1}, y_i, z_i)}{(\Delta x)^2} \\ & + \frac{B_z(x_i, y_{i+1}, z_i) - 2B_z(x_i, y_i, z_i) + B_z(x_i, y_{i-1}, z_i)}{(\Delta y)^2} \\ & + \frac{B_z(x_i, y_i, z_{i+1}) - 2B_z(x_i, y_i, z_i) + B_z(x_i, y_i, z_{i-1})}{(\Delta z)^2}\end{aligned}$$

where Δx, Δy and Δz are the distances between adjacent pixels in the x-, y- and z-directions, respectively. For each injection current between a chosen pair of electrodes, we also computed the voltage difference between the other pair of electrodes not injecting current and used these voltages to recover the absolute values in the reconstructed conductivity images by appropriate scalings.

Since the simulated measured data for B_z^j were available only for the region M, we could reconstruct the conductivity images only within the region M using the algorithm described in the previous section. However, during the iteration, we must know the conductivity distribution of the entire subject to numerically solve (10). Therefore, for each iteration, we set the conductivity distributions of the regions L and U as those of $\mathcal{S}_{M_1}$ and $\mathcal{S}_{M_{20}}$, respectively. We will discuss the implication of this approximation later in this paper.

In order to evaluate the performance of the algorithm against different amounts of measurement noise, we assumed SNRs of 15, 30, 60 and 90 in MR magnitude images. From the sensitivity analysis of the MRCDI technique by Scott *et al* (1992), these SNRs correspond to the noise standard deviations of 2.60, 1.30, 0.645 and 0.433 nT, respectively, in measured B_z^j data for injection current pulses with a duration of 48 ms. For each SNR,

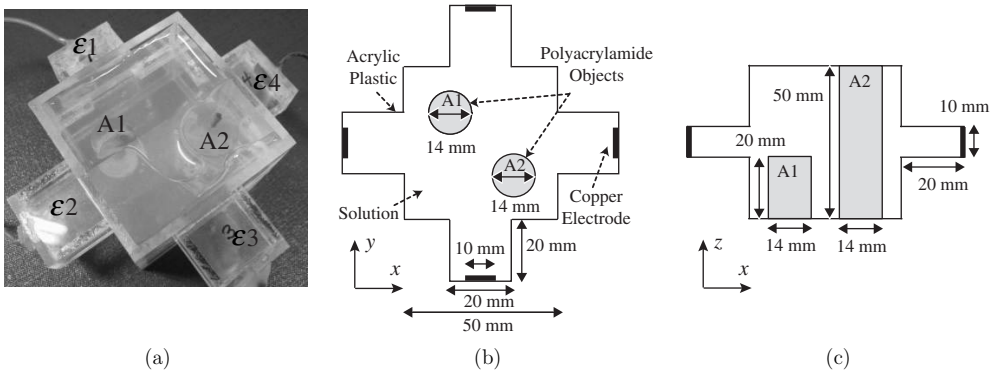

(a) (b) (c)

Figure 2. (a) Cubic saline phantom with four recessed electrodes used in experiments. Diagrams of the phantom: (b) top view and (c) front view (the recessed electrode on the front is hidden). The conductivity values of the solution, A1 and A2 were 2, 0.56 and 0.56 S m^{-1}, respectively.

we added the corresponding Gaussian random noise independently to each of all the B_z^j images so that all of them have different random noise patterns. In numerical simulations with added noise, we set the weighting matrix $\mathbf{W}$ as in (6).

We performed all numerical computations on a PC with an Athlon 2000+ processor, 1 GB RAM and Windows 2000 professional operating system using double precision floating point variables. Computing the numerical solution of (10) using the mesh with 254 400 elements and 268 309 nodes took about 5 min for each injection current. Since we solved (10) for six injection currents in every iteration, the computation time of one iteration was about 32 min.

2.4. Experimental methods

We constructed a cubic saline phantom of $50 \times 50 \times 50$ mm^3 shown in figure 2(a). On the four sides of the phantom, recessed electrode assemblies of $20 \times 20 \times 10$ mm^3 were positioned symmetrically. Within each recessed electrode assembly, we installed a copper electrode of 10×10 mm^2. The phantom was filled with a solution of 2 S m^{-1} conductivity (12.5 g l^{-1} NaCl and 2 g l^{-1} $CuSO_4$). Inside the phantom, we located two cylindrical objects (5 ml of 20% polyacrylamide, 4.9 ml of 6% sodium-styrenesulfonate with molecular weight of 70 000, 15 mg of $CuSO_4$, 0.1 ml of 10% ammonium persulfate and 4 μ l of tetramethylethylenediamine) denoted as A1 and A2 in figure 2. The measured conductivity values of A1 and A2 were 0.56 S m^{-1} 2 h after they were immersed in the solution. Their diameters were 14 mm and heights were 20 and 50 mm, respectively. Figures 2(b) and (c) show the diagrams of the phantom.

We put the phantom in our 0.3 T experimental MRI scanner. The main magnet of the MRI scanner was a permanent magnet with gap size of 500 mm and the main magnetic field pointed in the z-direction. We selected the first pair of electrodes to inject current I^1. The injection current pulses of 48 ms and 26 mA were synchronized with a standard spin echo MRCDI pulse sequence as described in Khang *et al* (2002) and Lee *et al* (2003a). After acquiring image data for the injection current I^1, we sequentially selected other pairs of electrodes and repeated the same data collection process for all six injection currents. When we injected current through a pair of electrodes, we also measured the voltage difference between the other pair of electrodes to which injection current was not applied.

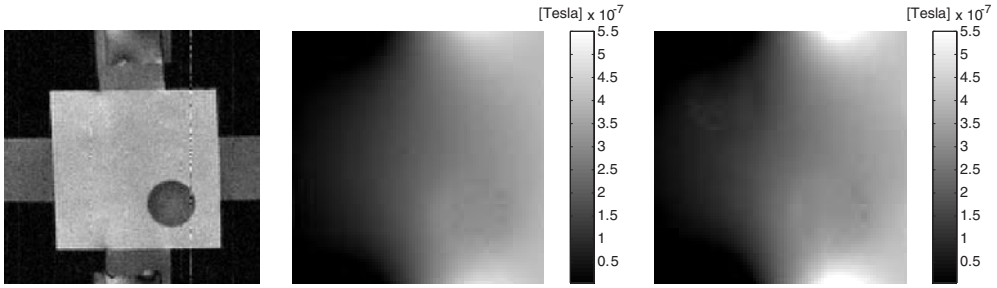

(a) (b) (c)

Figure 3. (a) MR magnitude image of the phantom with four recessed electrodes at the axial imaging slice of $\mathcal{S}_9$ ($25 \leqslant z \leqslant 28.1$ mm). Since the imaging slice is above the object A1 as shown in figure 2(c), we can see only the object A2. (b) 82×82 image of B_z^1 at $\mathcal{S}_{12}$. (c) 82×82 image of B_z^1 at $\mathcal{S}_6$.

We used a three-dimensional spin echo volume imaging sequence to obtain 16 axial images (xy-plane). The image matrix size was 128×128, the phase encoding step in the z-direction was 16, the number of averagings was 4, TR was 200 ms, TE was 60 ms, the field of view (FOV) in the x- and y-directions was 77 mm and the FOV in the z-direction was 50 mm. The slice thickness was 3.1 mm and pixel size was 0.6×0.6 mm^2. Average SNRs of magnitude images in the solution, A1 and A2 regions were 30.2, 13.6 and 13.6, respectively. We denote each imaging slice as $\mathcal{S}_i$ for $i = 1, \ldots, 16$ from the bottom to the top of the phantom. Figure 3(a) shows a typical MR magnitude image of the phantom at $\mathcal{S}_9$ ($25 \leqslant z \leqslant 28.1$ mm). We can see only the object A2 because $\mathcal{S}_9$ is above the object A1 as shown in figure 2(c). Since we were interested only in the internal region of the phantom, we extracted central 82×82 pixels corresponding to 50×50 mm^2 from all images for the subsequent data processing.

In order to compensate geometrical distortions caused by the main magnetic field inhomogeneity and gradient non-linearity, we applied the geometrical error correction method using a grid phantom as described in Khang *et al* (2002) and Lee *et al* (2003a). For the phase unwrapping, we used the Goldstein's branch cut algorithm (Ghiglia and Pritt 1998). It is a kind of path-following method and successfully unwraps noisy MR phase images. After the phase unwrapping, phase images were converted to magnetic flux density images of B_z^j by an appropriate scaling as described in Khang *et al* (2002) and Lee *et al* (2003a). Figures 3(b) and (c) show 82×82 images of B_z^1 for the injection current I^1 at the imaging slices of $\mathcal{S}_{12}$ and $\mathcal{S}_6$, respectively.

For the computation of the weight matrix $\mathbf{W}$, we first applied the total variation based denoising technique by Chan *et al* (2000) to all B_z^j images. Then, we considered these denoised images as noise-free images. For each B_z^j image, the amount of noise was estimated as the difference between the corresponding noise-free image and the original noisy image. This enabled us to compute the weight in (6) for each pixel in B_z^j images.

3. Results

3.1. Results of computer simulation

We set the conductivity distribution of the region M as shown in figure 4(a) with the average conductivity of 0.49 S m^{-1}. We assumed that two regions, U and M, were homogeneous with conductivity values of 0.97 and 0.24 S m^{-1}, respectively. Using the simulated data of

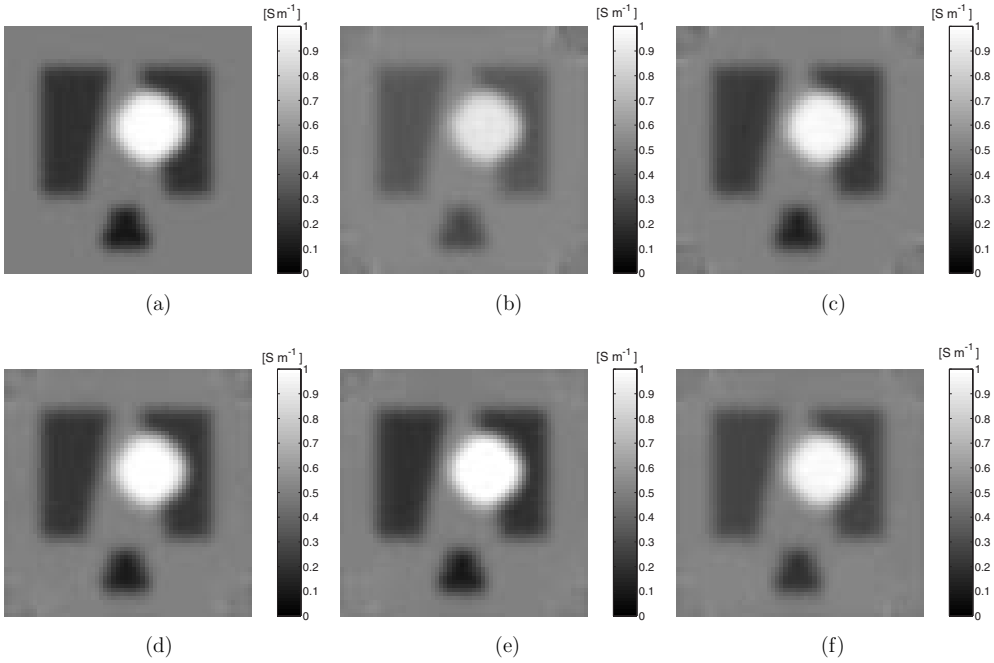

Figure 4. (a) True conductivity image. Reconstructed conductivity images without added noise in B_z at (b) $\mathcal{S}_{M_{20}}$, (c) $\mathcal{S}_{M_{15}}$, (d) $\mathcal{S}_{M_{10}}$, (e) $\mathcal{S}_{M_5}$ and (f) $\mathcal{S}_{M_1}$.

B_z^j with $j = 1, \ldots, 6$ from slices $\mathcal{S}_{M_i}$ with $i = 1, \ldots, 20$, we applied the $\nabla^2 B_z$ algorithm to reconstruct conductivity images in all 20 slices of the region M. Figures 4(b)–(f) show the reconstructed conductivity images at $\mathcal{S}_{M_{20}}$, $\mathcal{S}_{M_{15}}$, $\mathcal{S}_{M_{10}}$, $\mathcal{S}_{M_5}$ and $\mathcal{S}_{M_1}$, respectively, after six iterations. In step 5 of the algorithm described in section 2.2, the tolerance $\epsilon = 0.005$ was used. In order to express the accuracy of the reconstructed images, we defined the relative L^2-error ϵ_{σ_i} as

$$\epsilon_{\sigma_i} = \frac{\|\sigma - \sigma_i\|_2}{\|\sigma\|_2} \times 100\ [\%]$$

where σ_i is the reconstructed conductivity image at the slice $\mathcal{S}_{M_i}$ for $i = 1, \ldots, 20$ and σ is the true conductivity image shown in figure 4(a). Note that this L^2-error ϵ_{σ_i} is different from the tolerance ϵ used in the image reconstruction process. Figure 5 shows the plot of the relative L^2-errors.

Figures 6(a)–(d) show the reconstructed conductivity images at $\mathcal{S}_{M_{10}}$ with added Gaussian random noise corresponding to SNRs of 90, 60, 30 and 15, respectively, without using any denoising technique. With the tolerance $\epsilon = 0.005$, it took four iterations to reconstruct these images. The relative L^2-errors were 15.2, 16.1, 20.1 and 38.0%, respectively. Figures 7(a)–(e) show horizontal profiles of the reconstructed conductivity images at $\mathcal{S}_{M_{10}}$ for SNRs of infinity, 90, 60, 30 and 15, respectively.

After we reconstructed conductivity images at $\mathcal{S}_{M_i}$ for $i = 1, \ldots, 20$, we computed the current density image at $\mathcal{S}_{M_{10}}$ by solving (1) with σ replaced with the reconstructed values. The conductivity distributions in regions of L and U were filled with those of $\mathcal{S}_{M_1}$ and $\mathcal{S}_{M_{20}}$, respectively. Figures 8(a) and (b) show images of the magnitude of the true and reconstructed current density without added noise in B_z^j. The relative L^2-error between them was 3.98%.

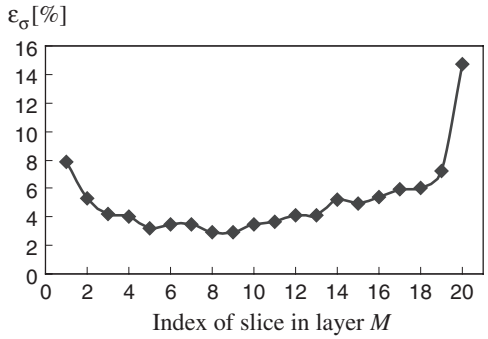

Figure 5. Relative L^2-errors of the reconstructed conductivity images from slices $\mathcal{S}_{M_i}$ for $i = 1, \ldots, 20$ without added noise in B_z.

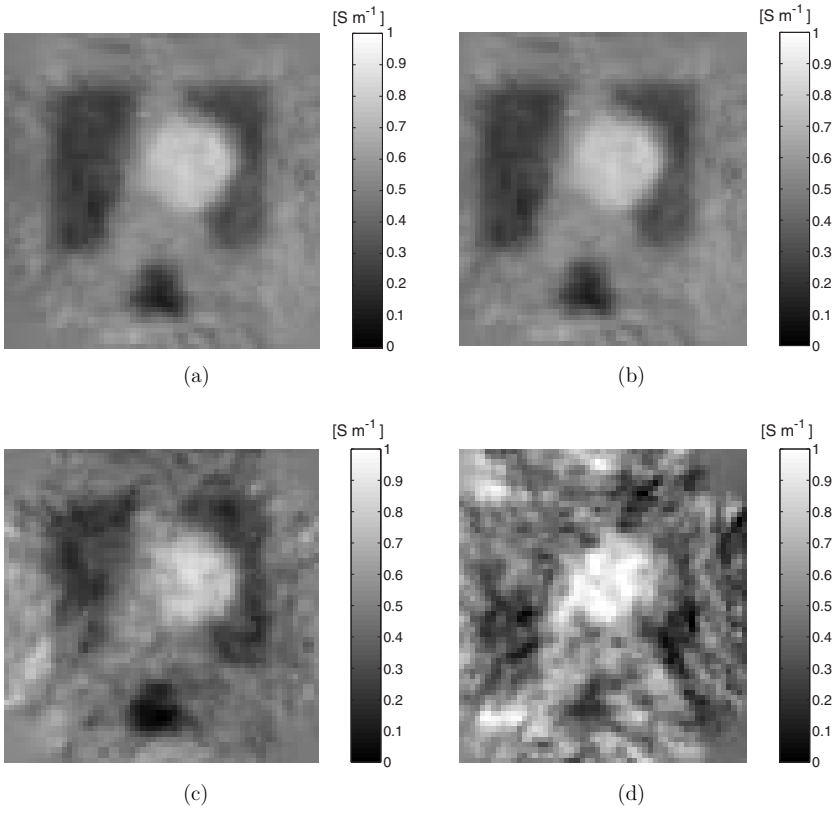

Figure 6. Reconstructed conductivity images at $\mathcal{S}_{M_{10}}$ with added Gaussian random noise in B_z corresponding to SNRs of (a) 90, (b) 60, (c) 30 and (d) 15. The relative L^2-errors are 15.2, 16.1, 20.1 and 38.0%, respectively.

With added Gaussian random noise, the relative L^2-errors between the true and reconstructed current density images were 6.86, 8.62, 17.0 and 33.5% for SNRs of 90, 60, 30 and 15, respectively.

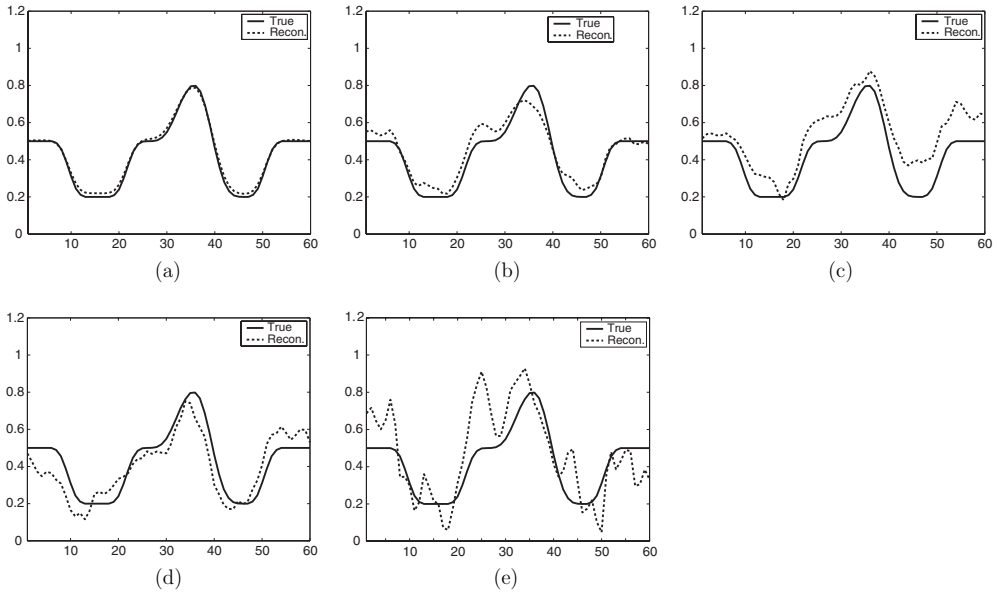

Figure 7. Conductivity profiles along the thirty-third row of $S_{M_{10}}$ with added Gaussian random noise in B_z corresponding to SNRs of (a) infinity, (b) 90, (c) 60, (d) 30 and (e) 15. Solid and dotted lines are the true and reconstructed profiles, respectively.

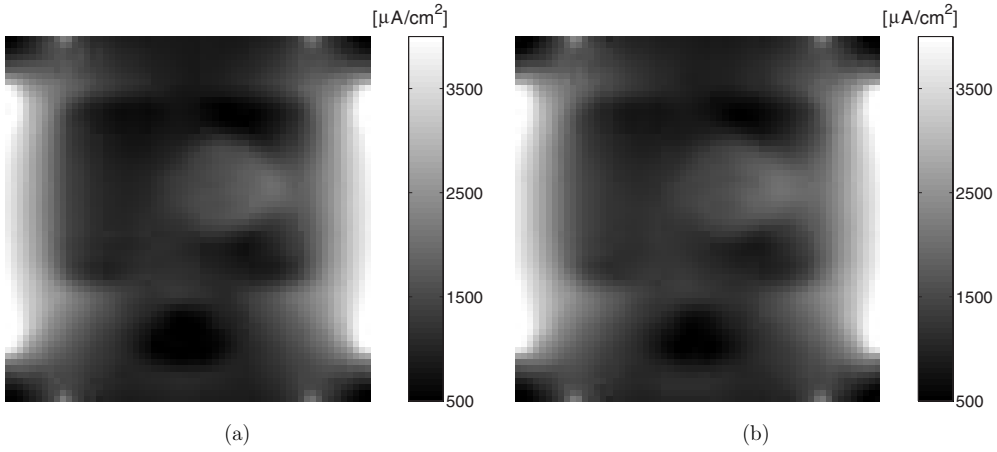

Figure 8. (a) True image of the magnitude of the current density distribution at $S_{M_{10}}$ for the horizontal injection current. (b) Corresponding reconstructed image at the same slice using the reconstructed conductivity values without added noise in B_z. The relative L^2-error between two images is 3.98%.

3.2. Experimental results

Using the measured B_z^j for $j = 1, \ldots, 6$, we applied the $\nabla^2 B_z$ algorithm to reconstruct conductivity images shown in figure 9. With the tolerance $\epsilon = 0.01$, it took six iterations to reconstruct these images. The relative L^2-errors of these images were between 13.8 and 21.5%. Figure 10 shows typical conductivity profiles of the reconstructed images in figure 9.

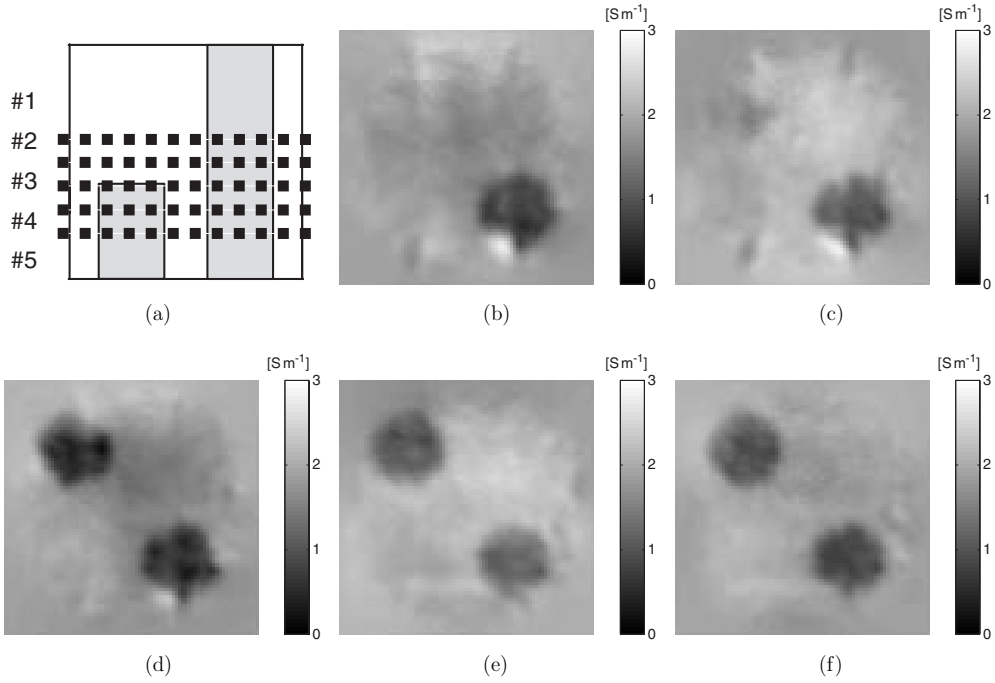

Figure 9. (a) Positions of five slices. Reconstructed conductivity images of the saline phantom at slices of (b) 1, (c) 2, (d) 3, (e) 4 and (f) 5. The relative L^2-errors are in the range 13.8–21.5%.

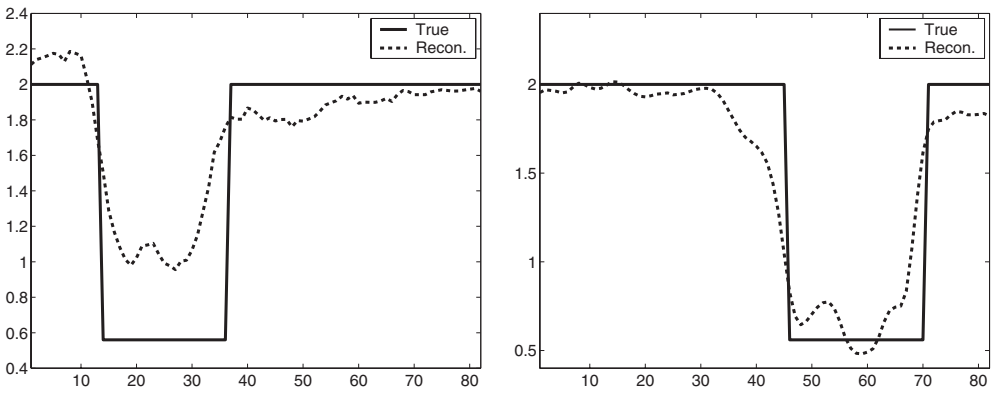

Figure 10. Typical horizontal profiles of the conductivity images in figure 9. Solid and dotted lines are the true and reconstructed profiles, respectively.

We solved (1) with σ replaced with the reconstructed values and computed current density distributions inside the phantom. Figure 11 shows two images of the magnitude of current density distributions. Figures 11(a) and (b) are current density images at two different slices including only the object A1 and both A1 and A2, respectively.

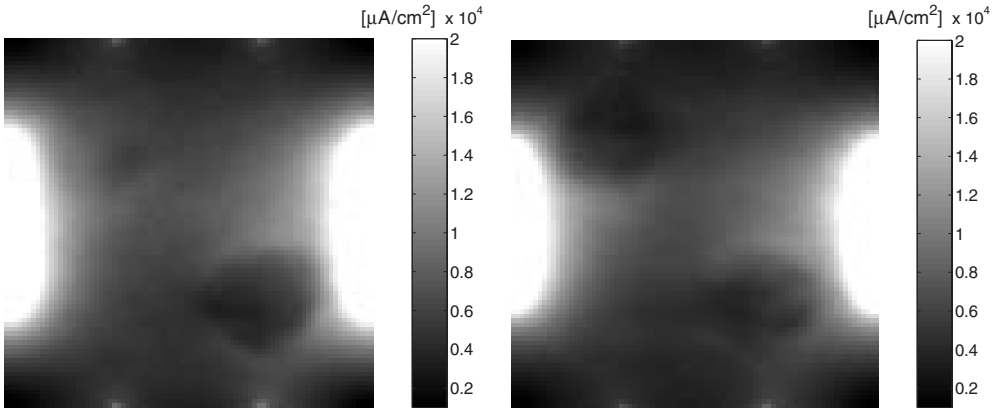

Figure 11. Typical reconstructed images of the magnitude of current density distributions. (a) Imaging slice $\mathcal{S}_9$ including only the object A1 and (b) different slice $\mathcal{S}_7$ including both A1 and A2.

4. Discussion

The $\nabla^2 B_z$ algorithm utilizes only the measured B_z data without using the impractical subject rotation procedure to obtain $\mathbf{B} = (B_x, B_y, B_z)$. Furthermore, it eliminates the effects of unknown lead wire geometry since the magnetic flux density $\mathbf{B}_I$ inside the subject due to the injection current I in external lead wires satisfies $\nabla^2 \mathbf{B}_I = 0$. This provides a significant convenience in the experimental procedure.

Simulation results without added noise show that the algorithm can successfully reconstruct both conductivity and current density images using only B_z data from multiple imaging slices. The only required approximation is in solving (10). We do not know the conductivity distribution of the entire subject unless we try a full three-dimensional conductivity image reconstruction over the entire subject. Therefore, we had to set the conductivity values in the region above (or below) the highest (or lowest) imaging slice the same as the highest (or lowest) slice. This causes more errors in upper and lower imaging slices compared to imaging slices at the middle. However, from the Biot–Savart law, the magnetic flux density at a field point due to a current density at a source point is inversely proportional to the square of the distance and proportional to the magnitude of the current density. When we inject currents using recessed electrodes as shown in figure 1(a), the current density in regions U and M is usually smaller than that in the region M. Therefore, the error due to this approximation is not significant in practical applications. The errors in figure 5 show asymmetrical increases as we move down or up from the centre slice. Since the true conductivity value in the region U was four times higher than that of the region L, the current density in U was larger than that in L. This explains larger errors in upper slices compared to lower slices. Nevertheless, we can see that the errors are small and minimal in slices at the middle.

The $\nabla^2 B_z$ algorithm requires the computation of $\nabla^2 B_z$ that is vulnerable to measurement noise. From computer simulation results, we could see that the SNR of the MR magnitude image should be greater than 30, for achieving less than 20% relative L^2-error in reconstructed conductivity images when the amount of injection current is 26 mA. Though using a denoising algorithm on measured B_z data may improve the accuracy at the expense of sacrificing some

edge information, we will still need to significantly decrease the amount of random noise to be able to reduce the amount of injection current. In addition to adopting a denoising algorithm, it would be desirable to devise a modified algorithm where we can reduce the number of differentiations to improve the noise tolerance.

Use of four recessed electrodes seems to be a good approach in terms of the following. First, it effectively moves the severe artefacts near copper electrodes away from the boundary of the subject. Second, it enables us to use the four-electrode method in measuring the boundary voltage data. Third, we can inject up to six different currents for collecting more information. Fourth, recessed electrodes with a known gel conductivity remove the requirement of boundary voltage measurements for recovering the absolute values of the conductivity images. Since we know the conductivity value of the gel within the recessed electrode assembly, this provides enough information to recover absolute values in reconstructed conductivity images. However, boundary voltages may help us in improving the accuracy of the reconstructed conductivity images if this additional information is correctly utilized during image reconstructions. We should further investigate the dimension and shape of the recessed electrode assembly for its optimal design.

We found that increasing the number of injection currents from the minimal value of 2 to N does not improve the condition number of $\tilde{\mathbf{U}}^T\tilde{\mathbf{U}}$ in (5). The condition number is strongly dependent on the pixel position rather than the number of injection currents. Since the condition numbers were much larger around four corners of the cubic subject, we used large values of the regularization parameter there. This resulted in more smoothed images around four corners in figures 4, 6 and 9. For the human subject, four wide recessed electrode assemblies would be desirable for minimizing the area of regions with very small current densities. Use of more than two injection currents is advantageous since it reduces the area of regions where measured B_z data are smaller than the noise level. When the SNR of MR magnitude image was 30, we found that use of six injection currents reduces the relative L^2-error by more than 30% compared with the result using two orthogonal injection currents I^1 and I^2 in figure 1(b).

In solving (5), we need to appropriately set weights w_j for $j = 1, \ldots, N$. This requires us to know the SNR of the measured B_z^j at every pixel. The method used in this paper is to estimate the noise by subtracting the measured B_z^j from the corresponding B_z^j after denoising using the total variation based method (Chan *et al* 2000). We need to further investigate other methods of estimating the SNR for each pixel. One possibility is to check the condition of $\nabla \cdot \mathbf{J} = 0$.

After we reconstruct the conductivity image σ, we can compute the current density images for any injection currents and electrode configurations. As described in the paper, we found that the reconstruction errors in the current density images were smaller than those of the conductivity images with added Gaussian random noise in B_z. This stems from the fact that we solve (1) with σ replaced by the reconstructed one to compute the current density, and (1) has a property of averaging errors in reconstructed conductivity values. The ability to compute the current density for any arbitrary current injection method will also be a valuable tool in many biomedical applications.

The computation time to solve (10) using a three-dimensional finite element mesh is the major factor determining the required time for image reconstructions. It will be necessary to reduce the amount of computation time using a non-uniform mesh and parallel computing with faster processors. Even though we reconstructed conductivity and current density images with a pixel size of $0.6 \times 0.6\,\text{mm}^2$, this does not correctly mean that the spatial resolution is $0.6 \times 0.6\,\text{mm}^2$. We need to further investigate the spatial and contrast resolution of the reconstructed images in terms of the mesh size, pixel size of MR images and full-width at

half-maximum (FWHM) values of point spread functions as was done in Birgul *et al* (2003). We will also study the effects of different numerical techniques and slice thicknesses in computing $\nabla^2 B_z$. A smaller slice thickness would be desirable especially when the conductivity rapidly changes along the z-direction. On the other hand, a larger slice thickness is advantageous in terms of the SNR.

In our future studies, we must find ways to reduce the amount of the injection current down to less than 1 mA for human subjects. We will look for better denoising methods and also try to enhance the SNR in measured magnetic flux density images. We suggest using an MRI scanner with a higher (for example, 3.0 T) main magnetic field. We will also investigate ways to reconstruct conductivity images only within a region of interest (ROI) where we have high enough SNR. In MREIT, MR magnitude images provide excellent structural information. We should devise a method to utilize this information probably linked with a certain regularization technique. We plan to undertake experiments involving animal subjects using a 3.0 T MRI scanner before applying the technique to human subjects.

5. Conclusion

Using the measured data of one component B_z of the induced magnetic flux density due to multiple injection currents, we found that the $\nabla^2 B_z$ algorithm successfully reconstructs both conductivity and current density images at several imaging slices lying on planes where current injection electrodes are placed. We used a 0.3 T experimental MRI scanner with 26 mA injection current for a subject with dimensions of $50 \times 50 \times 50$ mm^3. When the SNR of MR magnitude image was about 30 with a pixel size of 0.6×0.6 mm^2, relative L^2-errors of the reconstructed conductivity images were in the range of 13.8–21.5%.

In order to apply the technique to a larger subject with a reduced amount of injection current, we need to further investigate different ways of improving the SNR in measured magnetic flux density images. This may include an increased pixel size sacrificing some spatial resolution, an MRI scanner with a higher main magnetic field, better denoising methods, ROI imaging techniques, utilization of *a priori* structural information and others. Since this paper showed that only one component B_z is enough for both conductivity and current density image reconstructions in MREIT, our future study will be focusing on *in vitro* and *in vivo* experimental works with animal subjects.

Acknowledgment

This work was supported by the grant R11-2002-103 from Korea Science and Engineering Foundation.

References

Birgul O, Eyuboglu B M and Ider Y Z 2003 Current constrained voltage scaled reconstruction (CCVSR) algorithm for MR-EIT and its performance with different probing current patterns *Phys. Med. Biol.* **48** 653–71

Birgul O and Ider Y Z 1995 Use of the magnetic field generated by the internal distribution of injected currents for electrical impedance tomography *Proc. 9th Int. Conf. on Electrical Bio-impedance (Heidelberg, Germany)* pp 418–9

Boone K, Barber D and Brown B 1997 Imaging with electricity: report of the European concerted action on impedance tomography *J. Med. Eng. Tech.* **21** 201–32

Chan T, Marquina A and Mulet P 2000 High-order total variation-based image restoration *SIAM J. Sci. Comput.* **22** 503–16

Eyuboglu B M, Birgul O and Ider Y Z 2001 A dual modality system for high resolution–true conductivity imaging *Proc. 11th Int. Conf. Elec. Bioimpedance (ICEBI)* pp 409–13

Eyuboglu B M and Ozdemir M S 2003 Equipotential projection based magnetic resonance electrical impedance tomography (MR-EIT) and experimental realization *Proc. 4th Conf. Biomed. Appl. EIT (Manchester)* p 53

Eyuboglu B M, Reddy R and Leigh J S 1998 Imaging electrical current density using nuclear magnetic resonance *Elektrik* **6** 201–14

Eyuboglu B M, Reddy R and Leigh J S 1999 *Magnetic resonance-electrical impedance tomography* US Patent US6, 397, 095B1, issued on May 28, 2002

Folland G 1976 *Introduction to Partial Differential Equations* (Princeton, NJ: Princeton University Press)

Gamba H R, Bayford D and Holder D 1999 Measurement of electrical current density distribution in a simple head phantom with magnetic resonance imaging *Phys. Med. Biol.* **44** 281–91

Ghiglia D C and Pritt M D 1998 *Two-Dimensional Phase Unwrapping: Theory, Algorithms and Software* (New York: Wiley-Interscience)

Ider Y Z and Birgul O 1998 Use of the magnetic field generated by the internal distribution of injected currents for electrical impedance tomography (MR-EIT) *Elektrik* **6** 215–25

Ider Y Z, Muftuler T and Birgul O 1995 Use of MRI for measuring AC internal currents of EIT: a feasibility study *Proc. 9th Int. Conf. on Electrical Bio-impedance (Heidelberg, Germany)* pp 420–1

Ider Y Z, Onart S and Lionheart W R B 2003 Uniqueness and reconstruction in magnetic resonance–electrical impedance tomography (MR-EIT) *Physiol. Meas.* **24** 591–604

Joy M L G, Lebedev V P and Gati J S 1999 Imaging of current density and current pathways in rabbit brain during transcranial electrostimulation *IEEE Trans. Biomed. Eng.* **46** 1139–49

Kim S W, Kwon O, Seo J K and Yoon J R 2002 On a nonlinear partial differential equation arising in magnetic resonance electrical impedance tomography *SIAM J. Math. Anal.* **34** 511–26

Khang H S, Lee B I, Oh S H, Woo E J, Lee S Y, Cho M H, Kwon O, Yoon J R and Seo J K 2002 J-substitution algorithm in magnetic resonance electrical impedance tomography (MREIT): phantom experiments for static resistivity images *IEEE Trans. Med. Imaging* **21** 695–702

Kwon O, Lee J Y and Yoon J R 2002a Equipotential line method for magnetic resonance electrical impedance tomography (MREIT) *Inverse Problems* **18** 1089–100

Kwon O, Woo E J, Yoon J R and Seo J K 2002b Magnetic resonance electrical impedance tomography (MREIT): simulation study of J-substitution algorithm *IEEE Trans. Biomed. Eng.* **48** 160–7

Lee B I, Oh S H, Woo E J, Lee S Y, Cho M H, Kwon O, Yoon J R and Seo J K 2002 Three-dimensional forward problem in magnetic resonance electrical impedance tomography (MREIT) *Proc. 2nd Joint IEEE EMBS/BMES Conf. (Houston, TX)* pp 967–8

Lee B I, Oh S H, Woo E J, Lee S Y, Cho M H, Kwon O, Seo J K and Baek W S 2003a Static resistivity image of a cubic saline phantom in magnetic resonance electrical impedance tomography (MREIT) *Physiol. Meas.* **24** 579–89

Lee B I, Oh S H, Woo E J, Lee S Y, Cho M H, Kwon O, Seo J K, Lee J Y and Baek W S 2003b Three-dimensional forward solver and its performance analysis for magnetic resonance electrical impedance tomography (MREIT) using recessed electrodes *Phys. Med. Biol.* **48** 1971–86

Oh S H, Lee B I, Woo E J, Lee S Y, Cho M H, Kwon O, Yoon J R and Seo J K 2002 Magnetic resonance electrical impedance tomography (MREIT): phantom experiments for static resistivity images using J-substitution algorithm *Proc. 2nd Joint IEEE EMBS/BMES Conf. (Houston, TX)* pp 917–8

Saulnier G J, Blue R S, Newell J C, Isaacson D and Edic P M 2001 Electrical impedance tomography *IEEE Signal Process. Mag.* **18** 31–43

Scott G C, Joy M L G, Armstrong R L and Henkelman R M 1991 Measurement of nonuniform current density by magnetic resonance *IEEE Trans. Med. Imaging* **10** 362–74

Scott G C, Joy M L G, Armstrong R L and Hankelman R M 1992 Sensitivity of magnetic resonance current density imaging *J. Magn. Reson.* **97** 235–54

Seo J K, Yoon J R, Woo E J and Kwon O 2003 Reconstruction of conductivity and current density images using only one component of magnetic field measurements *IEEE Trans. Biomed. Eng.* **50** 1121–4

Webster J G 1990 *Electrical Impedance Tomography* (Bristol: Adam-Hilger)

Woo E J, Lee S Y and Mun C W 1994 Impedance tomography using internal current density distribution measured by nuclear magnetic resonance *Proc. SPIE* **2299** 377–85

Zhang N 1992 Electrical impedance tomography based on current density imaging *MSc Thesis* Department of Electrical Engineering, University of Toronto, Toronto, Canada